Bioactive Materials 50 (2025) 273–286

Contents lists available at ScienceDirect

Bioactive Materials

journal homepage: www.keaipublishing.com/en/journals/bioactive-materials

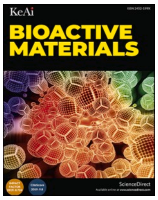

A double network composite hydrogel with enhanced transdermal delivery by ultrasound for endometrial injury repair and fertility recovery

Xin Zhang[a,b,1], Shufang Wang[c,1], Siyu Wang[a,b], Zeyi Long[a,b], Cong Lu[b,d], Jianlin Wang[a,b], Lijun Yang[a,b], Cancan Yao[a,b], Bin He[b], Xihua Chen[b,*], Taifeng Zhuang[e,**], Xiangbo Xu[b,***], Yufeng Zheng[f,****]

[a] Chinese Academy of Medical Science and Peking Union Medical College, Beijing, 100730, China
[b] NHC Key Laboratory of Reproductive Health Engineering Technology Research, Department of Reproduction and Physiology, National Research Institute for Family Planning, Beijing, 100081, China
[c] Department of Forensic Medicine, Xinxiang Medical University, Xinxiang, Henan, 453003, China
[d] Qingdao Blood Center, Qingdao, Shandong, 266071, China
[e] Beijing Obstetrics and Gynecology Hospital, Capital Medical University, Beijing, 100026, China
[f] School of Materials Science and Engineering, Peking University, Beijing, 100871, China

ARTICLE INFO

Keywords:
Endometrium regeneration
Double network hydrogel
Ultrasound cavitation effect
Transdermal delivery
Fertility recovery

ABSTRACT

Endometrial injury and resulting female infertility pose significant clinical challenges due to the notable shortcomings of traditional treatments. Herein, we proposed a double network composite hydrogel, CSMA-RC-Zn-PNS, which forms a physical barrier on damaged tissue through photo-crosslinking while enabling sustained release of the active ingredient PNS. Based on this, we developed a combined strategy to enhance transdermal delivery efficiency using ultrasound cavitation. *In vitro* experiments demonstrated that CSMA-RC-Zn-PNS exhibits excellent biosafety, biodegradability, and promotes cell proliferation, migration, and tube formation, along with antioxidant and antibacterial properties. In a rat endometrial injury model, the ultrasound cavitation effect was demonstrated to enhance transdermal delivery efficiency, and the ability of CSMA-RC-Zn-PNS to promote endometrial regeneration, anti-fibrosis and fertility restoration was verified. Overall, this strategy combining CSMA-RC-Zn-PNS hydrogel and ultrasound treatment shows promising applications in endometrial regeneration and female reproductive health.

1. Introduction

Infertility is a significant public health issue in modern society, with approximately one in six couples facing challenges related to fertility [1–3]. Endometrial injury is one of the primary causes of female infertility, often resulting from trauma, infection, and other factors [4,5]. The most common conditions related to endometrial damage are intrauterine adhesions (IUA) and thin endometrium (TE), and the mechanism was primarily characterized by damage to the basal layer of the endometrium, impaired self-repair functions, and excessive fibrous tissue proliferation, ultimately leading to amenorrhea, miscarriage, or even infertility [6,7]. The standard surgical treatment procedure for IUA currently employed in clinical practice is transcervical resection of the adhesion (TCRA), which has a notably high recurrence rate, up to 62.5 % in severe cases [8,9]. Additionally, some methods utilize physical barriers such as intrauterine devices (IUDs) or Foley catheter balloons [10], however, long-term use can lead to inflammation and often necessitates removal, potentially causing secondary injury [11]. Moreover, intrauterine infusion treatments using hormones [12], medications [13], and stem cells [14] have shown some effectiveness, while their

---

Peer review under the responsibility of editorial board of Bioactive Materials.

* Corresponding authors.

** Corresponding author.

*** Corresponding authors.

**** Corresponding author.

E-mail addresses: xhchen.bio@outlook.com (X. Chen), ztf19731972@126.com (T. Zhuang), xuxiangbo@nrifp.org.cn (X. Xu), yfzheng@pku.edu.cn (Y. Zheng).

[1] Equal contribution, Joint first authors.

https://doi.org/10.1016/j.bioactmat.2025.04.007
Received 25 December 2024; Received in revised form 9 March 2025; Accepted 4 April 2025

clinical application faces challenges due to low drug absorption, poor retention, significant side effects, and ethical concerns [15–17]. Therefore, there is an urgent need to develop a treatment material that can enhance drug absorption and create a biodegradable physical barrier in the damaged uterine cavity [18–20]. This material should promote endometrial repair and regeneration, improve receptivity, and reduce endometrial fibrosis, ultimately improving adverse pregnancy outcomes for IUA patients.

Hydrogel, a novel biomedical 3D culture material in regenerative medicine, is considered the most promising alternative to extracellular matrix (ECM) [21–24]. Hydrogel possesses absorbability, degradability, and biocompatibility, making it an excellent carrier for promoting cell growth, survival, morphogenesis, and maintaining internal environmental stability, in addition to facilitating cell differentiation and migration [25–27]. In recent studies hydrogels have been widely used for regeneration of tissues such as bone [28–30], myocardium [31–34] and epidermis [35–37]. Furthermore, the three-dimensional internal structure of hydrogels enables encapsulation of substances such as drugs, growth factors, estrogens, and cells, enhancing their bio-functionality [38,39]. In recent years, drug-delivering hydrogels have been utilized for the repair of endometrial damage [40–42]. Injectable and temperature-sensitive hydrogels [43–45] are typically injected into the uterus in a sol-gel state, forming a gel in situ. However, they often only adhere to the tissue surface, resulting in low efficiency and effectiveness in drug delivery. On the other hand, hydrogel microneedle patches [46–48] have been developed for endometrial repair, where the microneedle tip encapsulates the active ingredient and penetrates deep into the damaged stroma of the tissue. Nevertheless, microneedles often lack sufficient adhesion to tissues and can be easily dislodged by uterine peristalsis and contractions, resulting in secondary damage.

Herein, we present a double network hydrogel, CSMA-RC-Zn, was formulated by utilizing photo-crosslinking of chitosan methacrylate (CSMA) and secondary zinc-cross-linking of recombinant collagen type III (RC). Subsequently, the traditional Chinese medicine extract, *Panax notoginsenosides* (PNS), was loaded onto it to produce CSMA-RC-Zn-PNS hydrogel (Fig. 1A). Building on this photo-crosslinked hydrogel, ultrasonic treatment was introduced during the surgery procedure. An

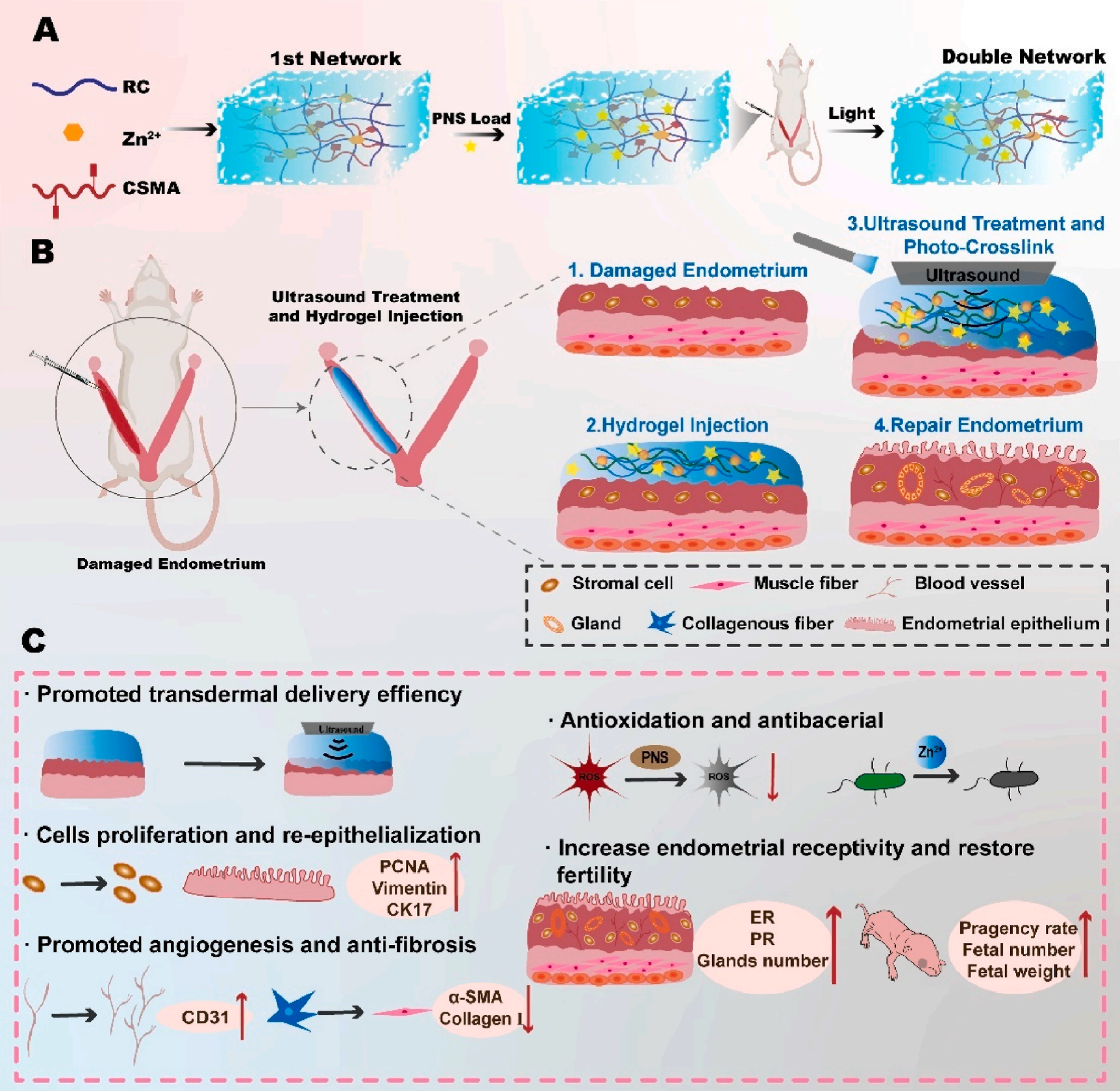

Fig. 1. Preparation of the hydrogel and its mechanism for endometrial regeneration. (A) Schematic illustration of the preparation of the CSMA-RC-Zn-PNS hydrogel. (B–C) CSMA-RC-Zn-PNS hydrogel promoted regeneration of injured endometrial in rats. CSMA-RC-Zn-PNS hydrogel with enhanced transdermal delivery by ultrasound can promoted cell proliferation and vascular regeneration, improved the inflammatory environment, and antibacterial, ultimately enabling effective repair and regeneration of the damaged endometrium, significantly enhancing the pregnancy rate.

ultrasound-mediated strategy for achieving tough bio-adhesion on tissue surfaces has been reported, with ultrasound-induced cavitation as the key mechanism [49]. This process propels and immobilizes the anchoring primer into the tissue by reducing the barrier effect, thus this strategy shows significant potential for transdermal drug delivery applications [50]. Collagen, a key component of the extracellular matrix, possesses biodegradable properties, low antigenic activity, low toxicity, and promotes cell growth. It has been successfully used in the repair and treatment of various tissues and organs [51–53]. However, most collagen currently in use is derived from animals, leading to significant batch-to-batch variability, challenges in isolating and purifying different types, and potential disease transmission risks [54]. Consequently, we chose recombinant collagen III produced through genetic engineering techniques which features a relatively simple structure, excellent biological compatibility, no viral potential, and low immunogenicity [55,56]. Considering the high fluidity, poor hydrolysis resistance, low osmotic pressure, and challenges in retaining the recombinant collagen solution through direct injection, we opted to cross-link it with other components to form a hydrogel for improved retention. Zinc ions (Zn^{2+}), recognized for their antibacterial and promote ECM synthesis properties, play a crucial role in wound healing [57–59]. Thus, Zn^{2+} can achieve enhanced pro-repair abilities by binding to RC through metal coordination [60,61], forming a first network and resisting conditions like bacterial infections. Chitosan, a deacetylated derivative of chitin, has been widely used in biomedical applications due to its biocompatibility, biodegradability and low immunogenicity [62,63]. CSMA with photo-crosslinked properties was the second network in the system that improved the internal structure of the hydrogel and enhances strength after injection into the injury site [64,65]. PNS is an important bioactive ingredient extracted from the traditional Chinese medicine *Panax notoginseng*, which has been reported to possess strong anti-inflammatory activity, hemostasis, antioxidant and immunomodulatory functions, and is effective in tissue repair and anti-tumor effects [66,67]. In conclusion, CSMA-RC-Zn-PNS can effectively promote the repair of damaged endometrial tissue and has antibacterial and antioxidant characteristics.

In this paper, we combine photo-crosslinked drug delivery hydrogel and ultrasound cavitation effects for endometrial injury repair. This strategy effectively improves transdermal drug delivery efficiency, enhances hydrogel adhesion to injured tissue, and creates a physical barrier at the injury site to prevent adhesions and secondary injuries. As illustrated in Fig. 1A–C, we prepared CSMA-RC-Zn-PNS hydrogel and verified its bio-safety and ability to promote cell proliferation, migration, and tube formation through *in vitro* experiments. Additionally, in a rat endometrial injury model, we confirmed that CSMA-RC-Zn-PNS enhances transdermal delivery efficiency under ultrasound cavitation, promotes proliferation, re-epithelialization, angiogenesis, reduces fibrosis in injured endometrial cells, and exhibits antioxidant and antimicrobial functions, ultimately improving uterine tolerance and restoring fertility.

2. Results and discussion

2.1. Preparation and characterization of the hybrid hydrogel

A two-step fabrication process was used for obtaining the CSMA-RC-Zn hybrid double network hydrogel. In brief, RC and Zn^{2+} were rapidly mixed to form the first network due to the Zn^{2+}-induced RC self-assembly. Then, CSMA was added into the first network and it can form the second network with visible blue light and LAP existed (Fig. 2A).

Fourier transform infrared spectroscopy (FT-IR, Fig. 2B) was performed to understand the chemical structure and confirm the successed construction of the hybrid hydrogel. The FT-IR spectrum of RC showed a broad band from 3629 cm^{-1} to 3116^{-1}, which was attributed to the stretching vibrations of N–H. The absorption peak at 1633 cm^{-1} was C=O stretching vibration indicating the formation of amide. In addition, the amide N–H and C–N vibration peaks were observed at 1531 cm^{-1} and 1236 cm^{-1}, respectively. The both groups of C=O and N–H are involved in the metal-ligand formation, however, the ratio of amide III and 1455.63 cm^{-1} was 0.849 and 0.846 for RC and RC-Zn, respectively. In general, an IR ratio of approximately 1 indicates the presence of helical structure. Due to the similarity of the IR ratio between RC and complex, it apparently had no pronounced effect on the helical structure

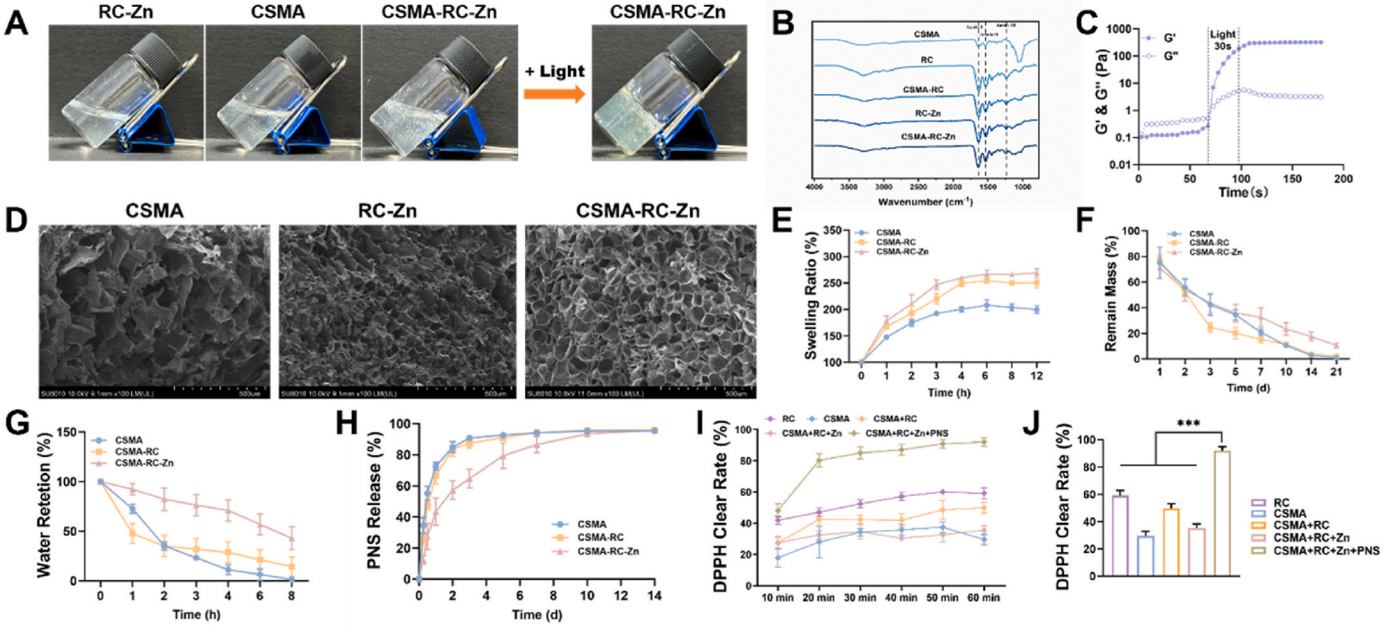

Fig. 2. Characterization of hydrogels. (A) Macroscopic changes of morphology during the preparation of hydrogels. (B) Infrared spectrum of the composite hydrogels. (C) Time-dependent rheological studies to evaluate the photo-enhanced mechanical property of the CSMA-RC-Zn hybrid hydrogel. (D) Microstructure of the hydrogels. (E–G) Water retention, swelling ration and degradation curve of the hydrogels. (H) The accumulated release rate of PNS from CSMA-RC-Zn hybrid hydrogel. (I–J) The clearance rate of DPPH by hydrogel, and DPPH radical scavenging curve of hydrogel with time.

of RC when zinc was incorporated.

Due to the photo-crosslink properties of CSMA, CSMA-RC-Zn precursor hydrogel solution can achieve a sol-gel transition rapidly with the 405 nm blue light existed. As evidenced by a rheological analysis (Fig. 2C), the storage modulus (G') increased and surpassed the loss modulus (G'') in less than 30 s with the light irradiation. Additionally, comprehensive rheological evaluations were conducted (Fig. S2), strain-sweep tests to delineate the linear viscoelastic region, frequency-sweep tests to quantify viscoelastic properties, shear-rate-dependent viscosity measurements to verify shear-thinning behavior, constant-shear viscosity analysis to assess hydrogel adhesive strength and strain-stress curve to assess hydrogel compress strength, thereby establishing a robust framework for systematic hydrogel performance assessment. Which show the linear viscoelastic region and modulus of the different hydrogels, verifying that the hydrogels have shear-thinning properties, as well as examining the viscosity of the different hydrogels. The combined data shows that the CSMA-RC-Zn dual network hydrogel has a wider linear viscoelastic region, can withstand higher stresses without deformation, has a lower relative strength, and has a higher viscosity.

The microstructures of the CSMA, RC-Zn, and CSMA-RC-Zn samples were observed by scanning electron microscopy (SEM, Fig. 2D). All the hydrogels had an internal three-dimensional pore structure, while CSMA-RC-Zn had a more uniform pore size and distribution (Fig. S3) which benefits to the future drug loading and delivery.

To better simulate the environment in which the hydrogels are exposed in the uterus and assess their performance, the simulated uterine fluid (SUF) was used in the swelling test and degradation test *in vitro* (Fig. 2E and F). All three hydrogel groups attained a quasi-equilibrium swelling state within 6 h. However, comparative analysis revealed that CSMA-RC-Zn-PNS exhibited a higher equilibrium swelling ratio than the other two hydrogels, and it can be attributed to the synergistic effects of its highly porous architecture and precisely modulated crosslinking density achieved through its double-network configuration. Notably, the degradation process of the hydrogels can be accelerated *in vitro* since the uterine and endometrial can squirm and contract, nevertheless, CSMA-RC-Zn was able to maintain a stable presence and

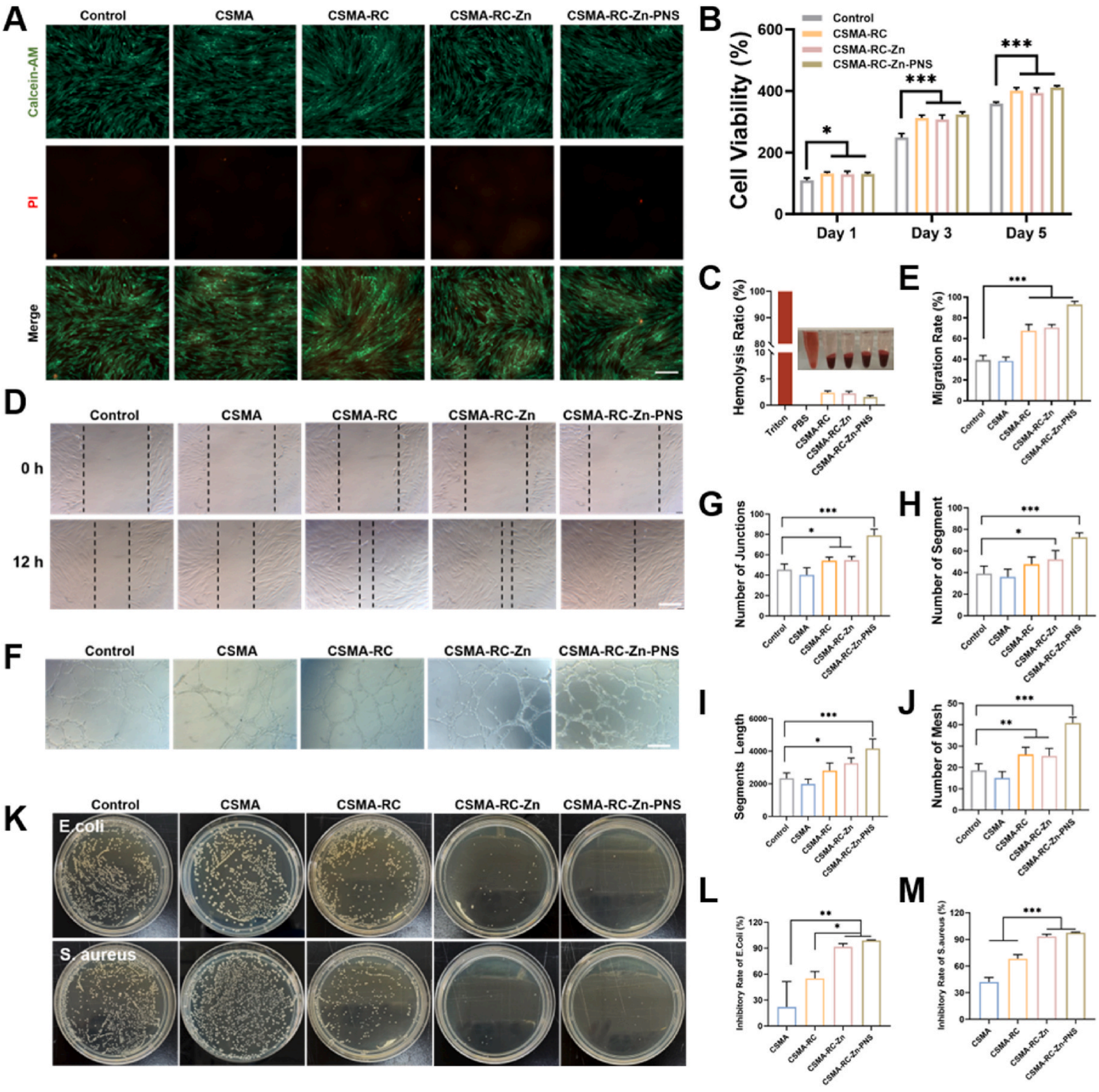

Fig. 3. Effects of hybrid hydrogels *in vitro*. A) Images showing the merged results of Live/Dead staining of HESCs treated with the extract of hydrogels for 5 days (n = 3). B) Proliferation assay of HESCs (n = 5). C) Hemolysis ratio of hydrogels exposure (n = 3). D-E) Images of the wound scratch migration assay and quantification of HESCs cells migration on hydrogels (n = 3). F-J)Tube formation and quantification analysis of HUVECs cultured over hydrogels (n = 3). K-M)Antibacterial properties of composite hydrogels: Colony count map and inhibitory rate of E. coli and S. aureus (n = 3).

continue to provide therapy during the repair cycle. Additionally, the water retention of hydrogels had been tested to access the stability in a dry wound environment, and the CSMA-RC-Zn demonstrated better performance in this test(Fig. 2G).

The *in vitro* PNS release profiles in different hydrogels also used the SUF as a simulated environment, PNS was rapidly released from the single network structure of CSMA and CSMA-RC hydrogels, as shown by the cumulative release curve(Fig. 2H), the release rate was already more than 70 % on the first day, with almost no sustained release after the third day. In parallel, the PNS release rate in CSMA-RC-Zn hydrogel was smoother that ensures a continuous supply of active ingredients during the damage repair cycle.

PNS is considered to be an herbal extract with antioxidant function, which is mainly achieved by scavenging excess free radicals from wounds, therefore we chose 1,1-diphenyl-2-picryl-hydrazyl radical (DPPH) reagent for free radical scavenging efficiency test (Fig. 2I and J). CSMA lacked noticeable antioxidant capacity, while the free radical scavenging efficiency of RC was difficult to meet the demand of damaged tissues, the loading and release of PNS significantly improved the free radical scavenging efficiency to 92.025 %.

2.2. *In vitro effects of the hybrid hydrogel*

For clinical wound repair application, favorable biocompatibility is a basic requirement for hydrogels. In order to evaluate the biocompatibility of the hydrogels and the effects they have on cellular behavior, the HESCs and HUVECs was used as the *in vitro* model cells. The Live/Dead staining assay was also performed after co-culture 1, 3 and 5 days, as shown in Fig. 3A–S4 and S5, most HESCs and HUVECs were alive (green fluorescence) with only a few dead cells (red fluorescence) present, indicating that the hydrogels could support cell adhesion and growth. The CCK8 assay was assessed by co-culture hydrogel extract with the cells for 1, 3 and 5 days, and the results showed that cell viability of the hydrogels compared to the control group was not decline, demonstrating the lack of cytotoxic effects (Fig. 3B and S6). At the same time, the cell viability increased and was significantly different from the control group in all hydrogel groups, indicating that the formulated hydrogels could promote cell proliferation.

Hemolysis rate was used to characterize the blood compatibility of hybrid hydrogels. The hemolysis rates of CSMA, CSMA-RC, CSMA-RC-Zn and CSMA-RC-Zn-PNS were all below the safe value of 5 % (Fig. 3C), indicated that the hydrogels satisfied the criteria for determining excellent blood compatibility.

Furthermore, the migration ability and angiogenic capacity was accessed. Upon scratch assay, CSMA-RC, CSMA-RC-Zn and CSMA-RC-Zn-PNS showed significantly faster migration rate since more cells migrated to the intermediate blank area, and the CSMA-RC-Zn-PNS group showed a closed trend after 12 h (Fig. 3D and E). For angiogenic evaluation, we cultured HUVECs on Matrigel with serum-free culture medium and hydrogel extract for 4 h and observed the tube formation (Fig. 3F). CSMA-RC-Zn and CSMA-RC-Zn-PNS hydrogels induced markedly more tube formation, not only in terms of junction numbers but also segments, tube length and mesh number (Fig. 3G–J). Excessive accumulation of reactive oxygen species (ROS) and pro-inflammatory macrophages at the wound site plays a pivotal role in the development and chronicity of wounds. Raw 264.7 cells were used to validate the free radical scavenging and antioxidant functions of hydrogels. The intracellular ROS levels in Raw 264.7 cells through external H_2O_2 supplementation. As shown in Fig. S7, CSMA-RC-Zn-PNS effectively reduced the fluorescence associated with reactive oxygen species, indicating its strong free radical scavenging and antioxidant properties. Overall, CSMA-RC-Zn-PNS can synergistically enhance the cell proliferation, migration, tube formation and antioxidant.

Bacterial infections are often a common trigger for endometrial injury and an obstacle to the healing process. *Staphylococcus aureus* (S. aureus) and *Escherichia coli* (E. coli) were used as experimental bacterial to study the antibacterial effect of hybrid hydrogels. Transition metal ions, such as Zn^{2+}, inherently possess antibacterial properties. The antibacterial efficacies of CSMA, CSMA-RC, CSMA-RC-Zn and CSMA-RC-Zn-PNS against S. aureus and E. coli were investigated using a coculture method and took images of bacterial coating plates. (Fig. 3K–M). CSMA-RC-Zn and CSMA-RC-Zn-PNS hydrogels showed superior antibacterial activity, achieving the bacterial killing ratio of 91.63 % and 99.05 % against E. coli and the bacterial killing ratio of 93.33 % and 97.63 % against S. aureus. This combinational antibacterial effect may be attributed to Zn^{2+} enhancing the bacterial membrane permeability, facilitating the entry of PNS into bacteria to exert its antibacterial effects.

2.3. *In vivo validation of the effect of ultrasound to enhance the efficiency of transdermal drug delivery*

The mechanism of ultrasound-enhanced transdermal delivery efficiency was showed in Fig. 4A, ultrasound (US)-induced cavitation effects lead to the rupture of microbubbles within the tissue matrix, creating tiny cavities. This process allows part of the solution on the tissue surface to be pushed into the tissue matrix. Subsequently, the solution's phot crosslinking properties are utilized to fix the hydrogel onto both the tissue matrix and the tissue surface, enhancing transdermal delivery efficiency and forming a physical barrier on the tissue surface. High temperature and pressure are generated during bubble rupture in the ultrasonic cavitation effect. Therefore, *in vitro* experiments were conducted to assess the temperature changes around the hydrogel under varying durations of ultrasonication, as Fig. S8 shown, continuous ultrasound for 60 s increases the temperature of the hydrogel solution by approximately 0.97 °C, while 180 s of ultrasound brings about a temperature increase of 2.2 °C, these temperature changes were safe for injured tissue and causes no additional damage. To verify that US can facilitate the entry of the solution into the tissue substate, the FITC-BSA labeled CSMA-RC-Zn hydrogel was used in the normal uterine and injury uterine separately. In the normal uterine (Fig. 4B), a portion of the green fluorescence penetrated the epithelial tissue into the stromal layer due to the ultrasound-induced cavitation. For the injury uterine, samples were collected at the in the immediate postoperative period and one day later (Fig. 4C). The uterine without US treatment was filled with hydrogels but it only adheres to the surface of the tissue and only a few green fluorescence could be seen in the stromal layer. However, the hydrogel not only remains in the uterine but also partially enters the uterine stromal layer and adheres tightly to the wound, the green fluorescence spreads significantly through the substrate after one day which indicated that US was able to deliver the solution transdermal to the endometrial stromal layer and ensure its firm adhesion to the injured tissue after gelation. The effect of varying durations of ultrasound treatment on drug delivery efficiency was also examined (Fig. S9). Results indicated that ultrasound treatments lasting more than 30 s significantly improved transdermal delivery efficiency, however, excessive duration could lead to secondary damage. Moreover, this strategy promotes prolonged and in-depth release of delivered drugs into injury tissues.

2.4. *Establishment of endometrial injury model and histological evaluation of uterine after different treatment*

The rats were sampled at different time points after injury surgery (Fig. 5A), and were randomly divided into five groups. In brief, the sham operation group was injected saline without injury to simulate the surgical procedure. Since the repair cycle after injury is divided into an acute inflammatory phase and a tissue repair phase, and taking into account that the cycle of physiological repair of the uterine is generally about 5–7 days. To validate the uniformity of model establishment across experimental groups, tissue samples were harvested from one randomly selected rat per group immediately following surgical

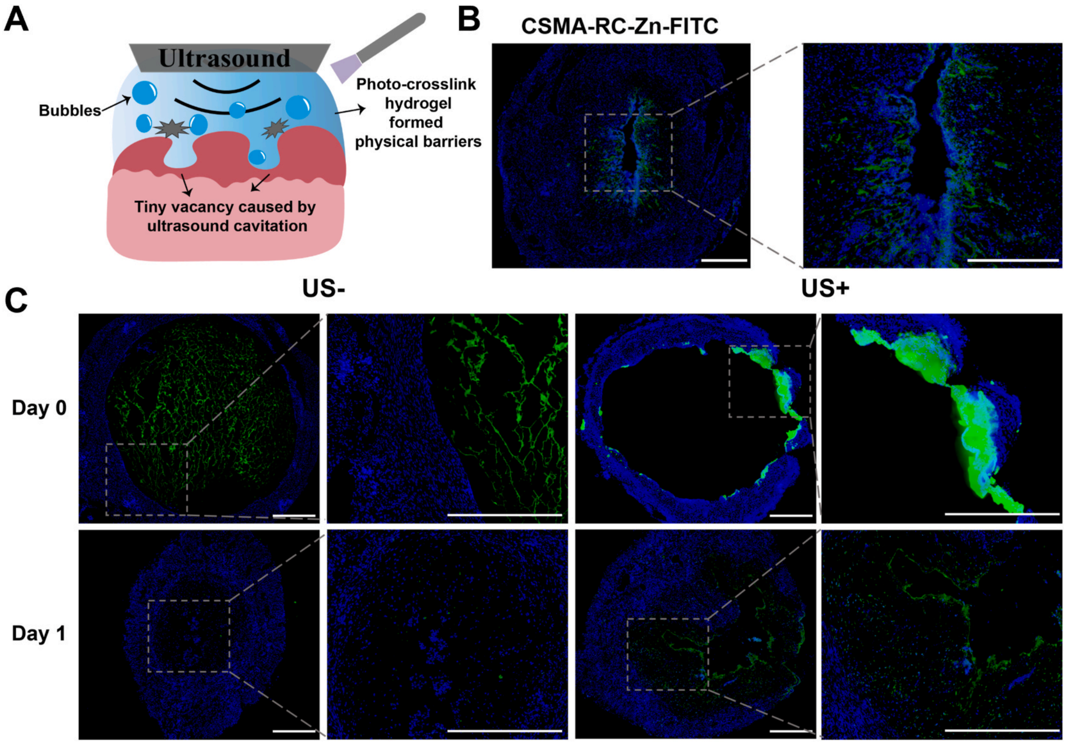

Fig. 4. *In vivo* validation of the effect of ultrasound to enhance the efficiency of transdermal drug delivery. A) Mechanism of ultrasound-induced increase in transdermal delivery efficiency. B)FITC-labeled CSMA-RC-Zn hydrogel injected into the normal uterus and delivery enhanced by ultrasound, images showed the distribution of fluorescence one day after surgery. C) Evaluation of the effect of ultrasound to improve transdermal delivery efficiency in a rat endometrial injury model. Bar = 400 μm.

intervention (postoperative day 0, Fig. S10). Five rats from each treatment group were executed at 3 and 7 days postoperatively, respectively. The gross morphometric picture (Fig. 5B and C) of the uterine after sampling shows that the uterine 3 days postoperatively of the control group was dark red, uneven thickness and inelastic with the presence of bruises while the uterine 7 days after the surgery wasn't much improvement and there was still bruising along with atrophy or effusion. Uterine damage was also more severe in the CSMA group taken 3 days postoperatively, with stiff endometrium and dark red bruising, while the uterine taken 7 days postoperatively had poorer elasticity and overall whiteness of the uterus. Some improvement in damage repair was noted in the CSMA-RC group, with a more uniformly thick and thin uterine despite bruising at 3 days postoperatively, and a pinkish-red and flexible uterus at 7 days postoperatively. In the CSMA-RC-Zn-PNS group, damage repair was faster and better than in the other treatment groups, and the uterine was already light pink with good elasticity 3 days after the operation, and the uterus was similar to the normal uterine in terms of thickness, shape and elasticity 7 days after the operation.

Morphological differences can be known from H&E staining (Fig. 5B and C) that the endometrium showed significant necrosis, severe stromal cell loss, and poor recovery at 7 days postoperatively of the control group. Stromal cell necrosis was also quite severe in the CSMA group, with no visible uterine structures in the uterus at 3 days postoperatively, and uneven endometrial thickness and incomplete epithelial coverage at 7 days postoperatively. Uterine stromal recovery was improved in the CSMA-RC group, with a significant increase in stromal cells and complete epithelial coverage seen at 7 days postoperatively, however there was a noticeable infiltration of inflammatory cells in the uterine. In the CSMA-RC-Zn-PNS group, the uterine cavity morphology was restored at 3 days postoperatively, and the stromal cells were tightly arranged with the epithelium was completely covered at 7 days postoperatively, inflammatory cell infiltration was also greatly improved. Specifically, in the sham group, the average endometrial thickness was 561.54 μm with 16.2 glands. However, in the control group the average thickness of the endometrium was 231.11 μm with only 2.4 glands and in the CSMA group the average thickness of the endometrium was 314.25 μm with an average of 5.4 glands. In the CSMA-RC group, the average thickness of the endometrium was 412.11 μm with an average of 9 glands. In contrast, the average endometrial thickness in the CSMA-RC-Zn-PNS group was 517.23 μm with an average of 15.6 glands, which demonstrated the remarkable capability of CSMA-RC-Zn-PNS to regenerate the injury endometrial (Fig. 5D and E). According to comprehensive analysis, CSMA-RC-Zn-PNS promoted the repair of damaged endometrium in a seven-day repair cycle, restored endometrial thickness and glandular counts to the equivalent level of a normal uterine, rebuild the structure of the uterine cavity and reduced the inflammatory response.

Besides, we established additional experimental cohorts including US-only treatment and CSMA-RC-Zn-PNS monotherapy (US-free) in rat endometrial injury models, with comparative analysis conducted against the original combination therapy group at postoperative day 7. Both control groups demonstrated significantly inferior repair efficacy compared to the CSMA-RC-Zn-PNS + US group (Fig. S11), particularly the US-only intervention showing minimal therapeutic impact. These findings demonstrate that CSMA-RC-Zn-PNS serves as an active hydrogel scaffold for endometrial repair, while ultrasound-mediated cavitation effects synergistically potentiate its therapeutic performance through enhanced transdermal delivery and tissue-material interaction. The complementary mechanisms between material design and physical energy modalities establish a novel combinatorial therapeutic paradigm.

2.5. *Assessment of endometrial collagen deposition and fibrosis after different treatment*

To further evaluate *in vivo* endometrial fibrosis in rats, we performed Masson's trichrome staining to examine collagen deposition in the endometrium across different groups (Fig. 6A). The ratio of blue color to

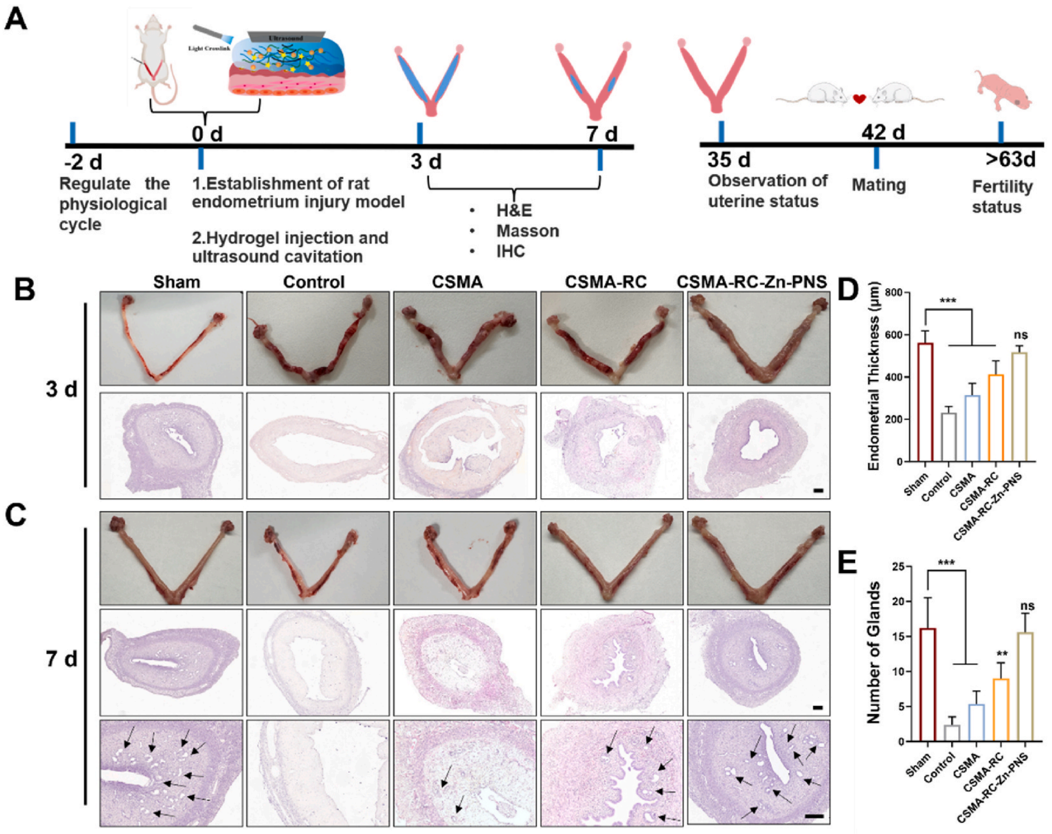

Fig. 5. The assessment of endometrial repair. A) Timeline of animal experiments based on endometrial regeneration and fertility restoration. B-C) Representative macroscopic and morphological changes at 3 and 7 days postoperatively in different groups. (The solid arrows pointed to the glands). D-E) The statistical graph of endometrial thickness and the number of glands at 7 days postoperatively in different groups. n = 10. Bar = 200 μm.

the total area in the staining results indicates the degree of uterine fibrosis. A universal increase in collagen deposition across all treatment groups compared to sham controls at postoperative day 3, corresponding to the initial phase of extracellular matrix remodeling. However, CSMA-RC-Zn-PNS showed significant lower collagen deposition level than other treatment groups. From the statistics at 7 days postoperatively, the average area of collagen deposition in the control group was 67.89 % while the average collagen deposition area in the CSMA and CSMA-RC groups was 55.98 % and 68.53 % separately. Notably, the average collagen deposition area in the CSMA-RC-Zn-PNS group was substantially lower at 27.84 %, nearly indistinguishable from the sham group at 26.885 %. The endometrial fibrosis markers Collagen I (Col I) and α-SMA were consistent with immunohistochemical staining of the uterine7 days after surgery. The Collagen I positive area was increased in the control group, CSMA group and CSMA-RC group but decreased in the CSMA-RC-Zn-PNS group (Fig. 6C) and the quantitative analysis showed significant differences (Fig. 6D). Similarly, the area positive for α-SMA was significant increase in the control group, CSMA group and CSMA-RC group, while it decreased in the CSMA-RC-Zn-PNS group (Fig. 6C–E). Notably, divergent trends were observed between Masson-stained collagen deposition levels and Col I, α-SMA positivity rates at the 7-day postoperative interval. While these three staining modalities collectively inform fibrotic progression assessment, their distinct biomarker signatures necessitate individual interpretation to comprehensively delineate therapeutic outcomes across experimental groups. Masson's trichrome staining primarily reflects total collagen deposition, serving to evaluate the extent of tissue fibrosis and reparative matrix accumulation. Col I immunohistochemistry specifically detects mature fibrillar collagen, with excessive expression indicating scar formation risk. α-SMA immunostaining identifies myofibroblasts, a key cellular marker of fibrotic progression. Notably, while the injury group exhibited elevated total collagen deposition via Masson staining, it demonstrated relatively lower Col I positivity and α-SMA expression compared to therapeutic groups. The CSMA-RC group showed predominant Col I deposition, indicative of advanced tissue remodeling. However, exceeding physiological levels implies potential scar predisposition, likely associated with dysregulated matrix synthesis pathways. Conversely, the CSMA group displayed heightened α-SMA positivity, reflecting myofibroblast hyperactivation and fibrotic contracture risks. Overall, the control group had immature extracellular matrix with delayed repair. And CSMA group showed fibrotic propensity through excessive myofibroblast activity. Meanwhile, CSMA-RC group showed structural restoration accompanied by scar formation alert. These findings highlight the delicate balance required in collagen homeostasis for functional tissue regeneration, where therapeutic strategies must concurrently suppress pathological fibrosis while guiding organized matrix deposition.

2.6. Assessment of the in vivo re-epithelialization, proliferation, angiogenesis and regeneration activity after different treatment

Clinically, re-epithelialization and revascularization of the exposed surface of the uterine are key factors for successful repair and remodeling of endometrium [16]. Immunohistochemical staining of CK17 was chosen as a marker for re-epithelialization which mainly located at luminal epithelium and glands in Fig. 7A. Evidently, the CSMA-RC-Zn-PNS group had epithelial cover 3 days postoperatively which other treatment groups lacked. At 7 days after surgery, the epithelium of all treatment groups recovered to a certain extent, but the positive signal area of CSMA-RC-Zn-PNS was still significantly higher than that of other groups, which proved that it could effectively promote endometrial re-epithelialization. The immunostaining of proliferation

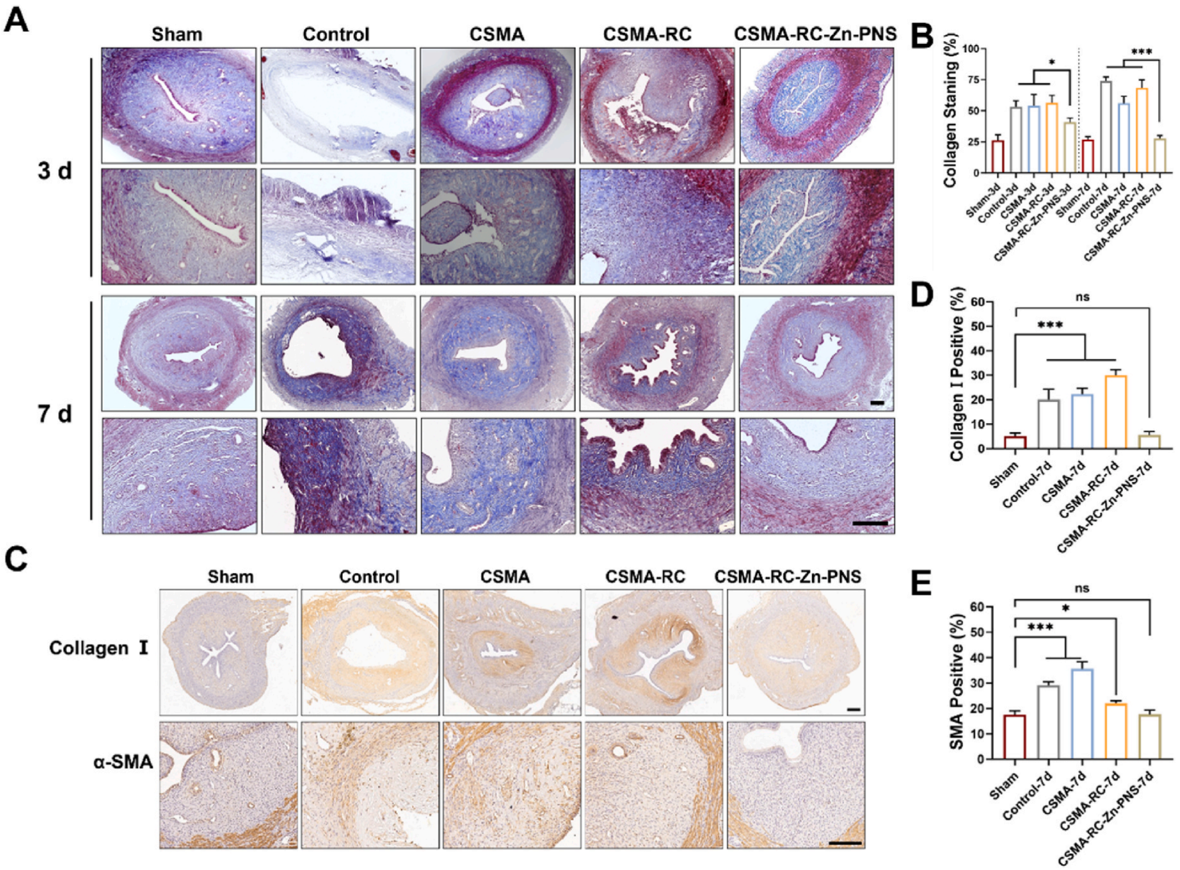

Fig. 6. *In vivo* effects of hydrogels in endometrial collagen deposition. A) The Masson's trichrome staining method was utilized to assess the presence of endometrial fibrosis. The blue color observed in the stained tissue sections is indicative of scar formation. Bar = 200 μm. B) Quantitative analysis of fibrosis area ratio. (n = 6). C) Representative immunohistochemical staining images at 7 days postoperatively of Collagen I and α-SMA as fibrosis markers. Bar = 200 μm. D-E) Quantitative positive area of Collagen I, α-SMA markers. (n = 6).

marker PCNA in the endometrial area revealed that CSMA-RC-Zn-PNS significantly promoted cell proliferation and wider distribution of cells in the tissue at both 3 and 7 days postoperatively (Fig. 7B). Angiogenesis has an essential role in the regenerative healing of injured uterine tissues, immunohistochemical staining of the rat uterus showed higher positive signal of CD31 in the CSMA-RC-Zn-PNS group compared to the other treatment groups at both 3 and 7 days postoperatively (Fig. 7C). In general, CSMA-RC-Zn-PNS was effective in promoting re-epithelialization, cell proliferation, and angiogenesis in the injured endometrium, thereby promoting endometrial regeneration and repair.

Furthermore, to validate the restoration of endometrial tolerance and functionality after surgery, the immunostaining of stromal cells marker (Vimentin), estradiol receptor marker (ER) and progesterone receptor marker (PR) were taken in the uterine at 7 days postoperatively. As shown in Fig. 7G, the vimentin positive signal in the CSMA-RC-Zn-PNS group was almost recovered to the level of the sham group while other treatment groups still had significantly fewer stromal cells. ER and PR are expressed in the nuclei of endometrial epithelial cells and stromal cells and play key roles in the regulation of reproduction, including menstruation and pregnancy. Since the stromal and epithelial cells in the CSMA-RC-Zn-PNS group recovered better, the expression levels of ER and PR were also more similar to those of the sham group. Overall, uterine tolerance and functionality were better restored in the CSMA-RC-Zn-PNS group, which facilitated the uterus to be able to conceive and give birth normally in the later stages.

2.7. *Assessment of fertility, live birth, and hydrogel safety after different treatment*

Restoration of fertility is considered the ultimate purpose of repair and regeneration of damaged endometrium, therefore, a series of experiments were used to validate postoperative fertility recovery in each treatment group. Five weeks postoperatively, eight rats in each treatment group were anesthetized with isoflurane and the abdominal cavity was opened to expose the uterus and photographs were taken to observe their gross morphology (Fig. S12). Varying degrees of effusion or atrophy occurred in the uterus of the control group, and to a lesser extent in the CSMA group, the uterus of the CSMA-RC group had no significant abnormalities in general but was dark reddish in color, however the uterine morphology of the CSMA-RC-Zn-PNS group was more similar to that of the sham-operated group, with no significant trauma or abnormalities. After suturing and continued rearing for one week, these female rats were mated 1:1 with SD males and mating success was verified by means of vaginal smears. Each treatment groups were sampled on the 21st day after conception to count the pregnancy rate, the number of fetal rats and fetal weights, as well as the heart, liver, spleen, lungs, kidneys and blood of female rats. Three of the female rats in each group were sacrificed before giving birth, and fetal rats were extracted and examined for stillbirths, absorbed fetuses, or malformations. One rat in the CSMA group had a stillborn fetus in uterine and one rat in the CSMA-RC group had an absorbed fetus in uterine (Fig. S13) and there were no abnormalities in fetal rats in the sham group and CSMA-RC-Zn-PNS groups. (Fig. 8C). The other five rats in each group produced naturally and counted overall normal pregnancy rate. The pregnancy rate was 100 % in the sham group compared to 0 % in the control group, and only

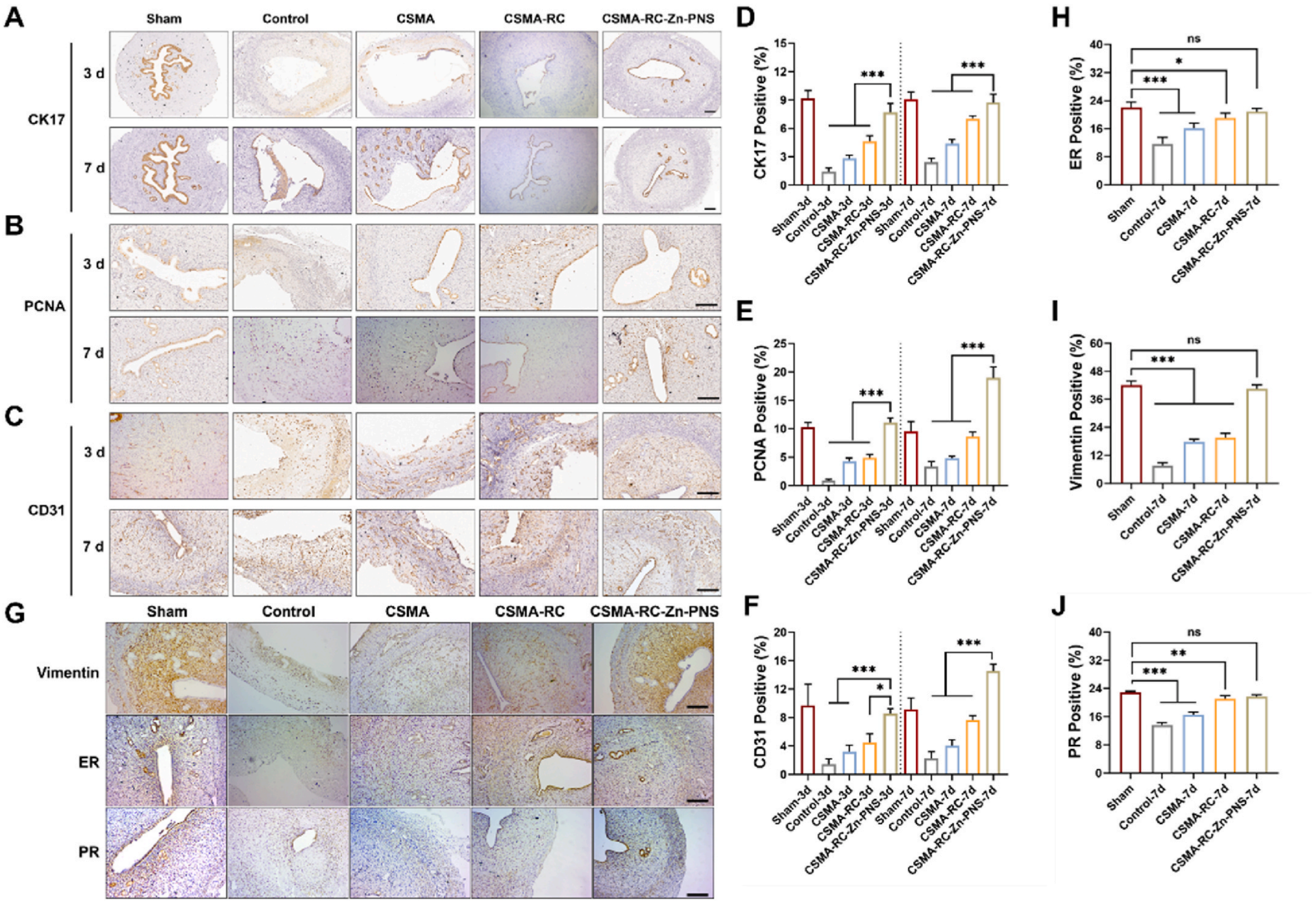

Fig. 7. *In vivo* effects of CSMA-RC-Zn-PNS in endometrial re-epithelialization, proliferation and angiogenesis. A-C) Representative immunohistochemical staining image of CK17 as a re-epithelialization marker, PCNA as a proliferation marker, CD31 as an angiogenesis marker at 3 and 7 days postoperatively in different groups. Bar = 200 μm. D-E) Quantification positive area of CK17, PCNA and CD31 marker. n = 6. G-J) Representative immunohistochemical staining image and quantification of vimentin as an endometrial stromal cells' marker, ER as an estradiol receptor marker and PR as progesterone receptor marker. n = 6. Bar = 200 μm.

12.5 % in the CSMA group, while the pregnancy rate was 75 % in both the CSMA-RC and CSMA-RC-Zn-PNS groups (Fig. 8B). The CSMA group had a significantly lower number of 4 embryos compared to the sham group of 12.17. On the other hand, the CSMA-RC group had an average number of 6.17 embryos while the CSMA-RC-Zn-PNS group had 9.83 embryos which was closer to the data of the sham group (Fig. 8D). The body weights of the fetuses were examined, and the average body weight was 5.98 g in the sham group, 5.64 g in the CSMA-RC group, and 5.91 g in the CSMA-RC-Zn-PNS group, while the CSMA group showed a significant decrease in body weight to 3.26 g (Fig. 8F). In addition, the development of offspring in the sham group, CSMA-RC group and CSMA-RC-Zn-PNS group were monitored, during the subsequent 14-day growth cycle, the fetal rats grew up healthily with no malformations or deaths (Fig. 8E).

In addition, blood biochemical tests for liver and kidney function (Fig. 8G–J) and Elisa tests for inflammatory factors (Fig. S14) were performed on serum collected from female rats. Serum creatinine and urea nitrogen were used to assess maternal kidney function, as well as ALT and AST to assess maternal liver function. The results showed no statistical difference of the four indicators in each treatment group, which proved that there was no abnormality in the liver and kidney functions of the female rats. Meanwhile, inflammatory levels of IL-6, IL-1β, and TNF-α were examined, and there were also no significant differences between the groups, demonstrating that there is no significant long-term biotoxicity *in vivo* for the materials in each group. Furthermore, H&E staining sections of the heart, liver, spleen, lungs and kidneys also showed no lesions or other abnormalities in the female rats of each treatment group (Fig. S15). Basically, the female rats in all groups were in a relatively healthy state, with no factors affecting fertility other than the uterine damage repair treatment.

3. Conclusion

This study presents an innovative injectable double-network composite hydrogel (CSMA-RC-Zn-PNS) aimed at promoting endometrial regeneration and improving fertility recovery. Simultaneously, the ultrasonic cavitation effect will enhance the efficiency of transdermal drug delivery *in vivo* when sonication is applied to the hydrogel. CSMA-RC-Zn forms a dual-network structure via metal coordination and photo-crosslinking, ensuring an optimal pore structure for loading the drug PNS while facilitating its sustained release during tissue repair. CSMA-RC-Zn-PNS hydrogel forms an adhesive layer on the surface of the injured tissue, creating a physical barrier that protects the wound from secondary injury and bacterial infection. Meanwhile, CSMA-RC-Zn-PNS demonstrates good biosafety, and its ability to promote cell proliferation, angiogenesis, re-epithelialization, and other aspects of tissue regeneration was confirmed through *in vitro* cell studies and rat endometrial injury models. Moreover, the cavitation effect facilitated the penetration of some of the solution into the tissue matrix, enhancing the absorption and utilization of the active ingredients, thereby improving the reparative effect of the hydrogel. Overall, the combined application of CSMA-RC-Zn-PNS hydrogel and ultrasonic cavitation effectively

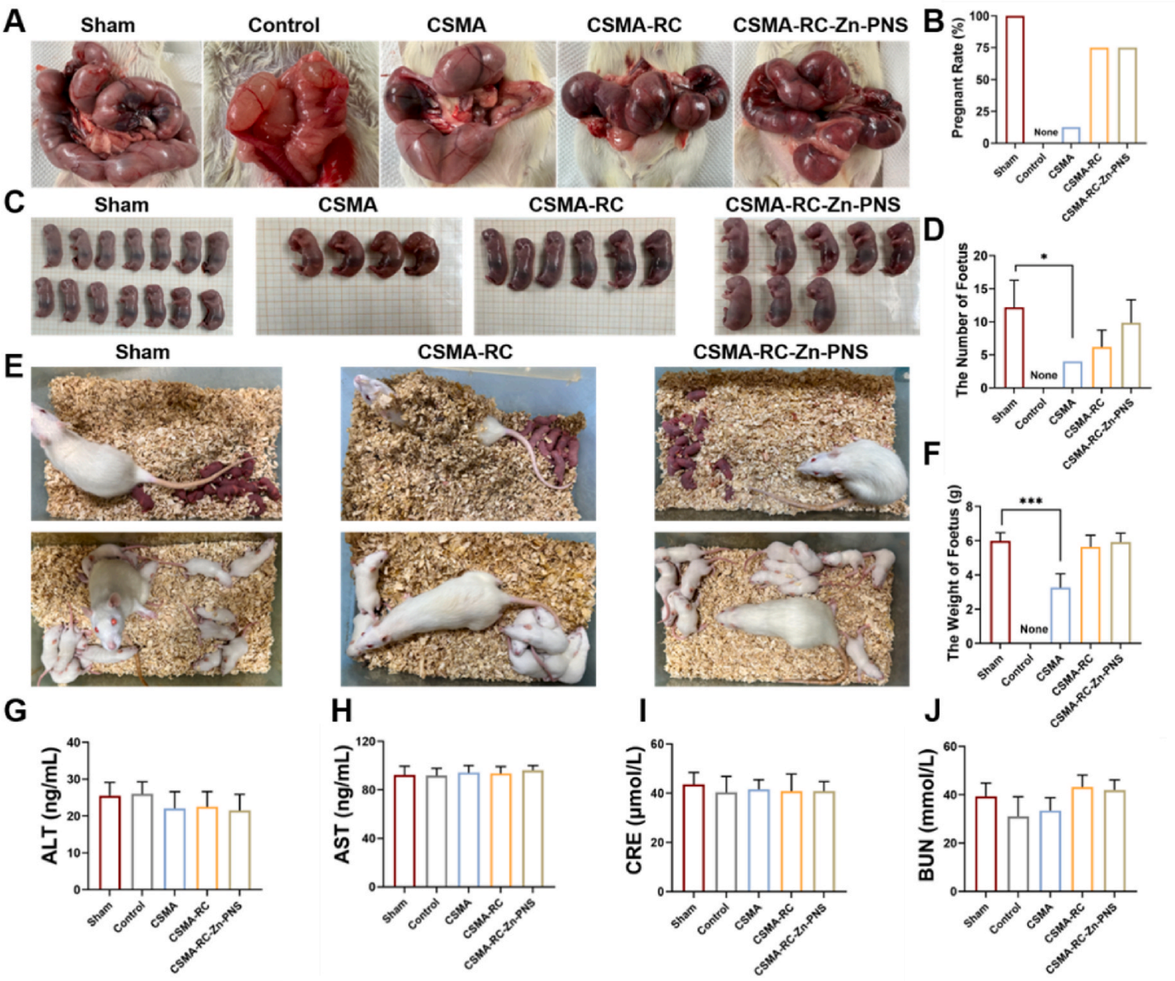

Fig. 8. Pregnancy outcomes of different interventions and hydrogel safety assessment. A) State of the rat uterus at 21 days of fertilization. B) The pregnant rate of different groups. C) The images showed fetuses of different groups. D) The number of fetuses of different groups. E) Photographic images of newborn rats and after feeding 14 days. F) The weight of fetuses of different groups. G-J)The statistical graphs of serum creatinine, urea nitrogen, ALT, and AST in maternal rats, respectively.

promotes endometrial injury repair and fertility restoration, offering promising prospects for clinical applications in endometrial recovery.

4. Experimental section

4.1. Materials

Chitosan, methacrylic anhydride, ethanol and zinc sulfate (99 %) were purchased from Sigma Aldrich (USA). Recombinant type III collagen (RC) was purchased from Shanxi Jinbo Bio-Pharmaceutical Co. Ltd (China). Panax notoginsenosides (PNS, UV ≥ 90 %) was purchased from Shyuanye Bio (Shanghai, China). Lithium phenyl (2,4,6-trimethylbenzoyl) phosphinate (LAP, 99.8 %) was purchased from EFL-Tech (Suzhou, China). The Cell Counting Kit-8 (CCK-8) assay kit, Calcein-AM/PI Live-Dead Cell staining kit, Triton X-100, Elisa kit was purchased from Solarbio Science & Technology (Beijing, China). Matrigel matrix was procured from Corning (USA). Dulbecco's modified Eagle's medium/Nutrient Mixture F-12 (DMEM/F12), Fetal Bivone Serum (FBS) was purchased from Gibco (USA). Endothelial Cell Medium (ECM), Penicillin/Streptomycin solution (P/S), Endothelial Cell Growth supplement (ECGS) was purchased from ScienCell (USA). 1,1-Diphenyl-2-picrylhydrazyl radical 2,2-Diphenyl-1-(2,4,6-trinitrophenyl)hydrazyl (DPPH) and 2′,7′-dichlorofluorescein diacetate (DCFH-DA) were purchased from Beyotime Biotechnology (Shanghai, China). Blood biochemistry kits were purchased from Njjcbio (Nanjing, China). All chemical reagents were used without further purification.

4.2. Cells and animals

Human endometrial stromal cells (HESCs), human umbilical vein endothelial cells (HUVECs) and RAW264.7 macrophage cells were purchased from the National Experimental Cell Resource Sharing Platform. Staphylococcus aureus (S. aureus, ATCC 25923) and Escherichia coli (E. coli, ATCC 25922) were used for the antibacterial studies. Sprague-Dawley (SD) rats (8–9 weeks old, female) were obtained from Beijing HFK Bioscience CO., Ltd. All protocols for animal care and treatment were approved by the Ethical Committee of National Research Institute for Family Planning (NRIFH 21-2308-3).

4.3. Synthesis of RC-Zn, CSMA-RC, CSMA-RC-Zn, CSMA-RC-Zn-PNS

1g RC was dissolved in 10 mL deionized water and then stirred for 30 min to form 10 wt% RC solution. Zinc sulfate solution (100 μg/mL) was added into the RC solution and stirred for 2–3h at room temperature to obtain RC-Zn. CSMA was synthesized according to previous studies and dissolved in deionized water to form 5 wt% CSMA with 0.1 wt% LAP. CSMA-RC was synthesized by mixing RC solution and CSMA solution according to the ratio 1:1 and stirred for 60 min at 4 °C in the dark.

Meanwhile, CSMA-RC-Zn precursor hydrogel solution was synthesized by mixing RC-Zn solution and CSMA solution according to the ratio 1:1 and stirred for 60 min at 4 °C in the dark. Subsequently, PNS solution (10 mg/mL) was added to CSMA-RC-Zn to form CSMA-RC-Zn-PNS precursor hydrogel solution, followed by ultrasonic dispersion. Then, the hydrogel system was irradiated by a visible light (405 nm, 5 W) for 60 s.

4.4. Characterization

The structure and architecture of the freeze-dried hydrogels were observed using SEM (SU8010, Hitachi, Japan). Structural and functional group analyses of the RC, CSMA and $ZnSO_4$ powders and the freeze-dried CSMA-RC, CSMA-RC-Zn hydrogels were recorded by Fourier transform infrared spectroscopy (FT-IR, VERTEX 70, Bruker, Germany) in the range 4000 - 600 cm^{-1}.

4.5. Rheological testing of the hydrogel

Rheological Characterization of Photopolymerization Processes: Hydrogel solutions (1 mL) were carried out on a stress-controlled Discovery DHR-2 rheometer (TA Instruments, USA) with time sweep. The alternant strain sweep of hydrogels was carried out at alternant strains of 1 %. The test was performed at room temperature and the angular frequency was fixed at 5 rad/s.

Strain sweep measurement: Hydrogels ($1cm^2 \times 1$ mm) was mounted on the rheometer stage, and strain sweep tests (0.1 %–100 %) were performed to monitor the evolution of storage modulus (G′) and loss modulus (G’’), with angular velocity maintained at 5 rad/s throughout the measurement.

Frequency sweep measurement: Hydrogels ($1cm^2 \times 1$ mm) was mounted on the rheometer stage, and frequency sweep tests (0.1–100 rad/s) were performed to monitor the evolution of storage modulus (G′) and loss modulus (G’’), with strain maintained at 1 % throughout the measurement.

Shear-thinning characteristic: Hydrogels ($1cm^2 \times 1$ mm) was mounted on the rheometer stage, and strain sweep tests (0.1 %–100 %) were performed to monitor the evolution of viscosity.

Viscosity: Hydrogels ($1cm^2 \times 1$ mm) was mounted on the rheometer stage, and shear rate maintain at 0.1/s throughout the measurement to evaluate the viscosity, and perform the calculation of the average value.

Strain-stress measurement: Hydrogels ($1cm^2 \times 1$ mm) was mounted on the rheometer stage, and strain sweep tests (0.1 %–3000 %) were performed to monitor the evolution of shear stress.

4.6. The swelling and degradation behavior of the hydrogels in vitro

The gravimetric method was used to test the swelling ratio and water retention of different hydrogels. The simulated uterine fluid was used to simulate the real physiological environment in rat uterus [68], and the configuration method is shown in the Supplementary Material. A certain mass (W_0, 1 g) of hydrogels were soaked in 10 mL simulated uterine fluid at 37 °C. The swollen hydrogels were taken out and weighed (W_t) at different time points. The swelling ratio was calculated by the following equation:

$$\text{Swelling Ratio } (\%) = W_t / W_0 * 100.$$

For the water retention test, a certain mass (M_0, 1 g) of hydrogels were put in the centrifuge tube and dried in the 37 °C environments, and the mass of different time points was measured (M_t). Water Retention was calculated by the following equation:

$$\text{Water Retention } (\%) = M_t / M_0 * 100.$$

The degradation property was carried out in a similar way. A certain mass (W_i, 1 g) of hydrogels was soaked in 10 mL simulated uterine fluid at 37 °C. The centrifuge tube was centrifuged and the mass of remain hydrogel (W_r) was measured at different time points. Then 10 mL simulated uterine fluid was added again. The remaining mass ratio was calculated by the following equation:

$$\text{Remaining Mass } (\%) = W_r / W_i * 100.$$

The test was repeated three times.

4.7. In vitro release analysis of PNS

A certain mass (1 g) of CSMA-RC-Zn-PNS hydrogels were was soaked in 10 mL simulated uterine fluid at 37 °C, the centrifuge tube was centrifuged and the solution was taken out at different time points. The cumulative release rate of PNS was measured using the vanillin-perchloric acid colorimetric method. After evaporating the solvent, 0.2 mL of 5 % vanillin-glacial acetic acid and 0.8 mL of perchloric acid were added. The mixture was heated in a thermostatic water bath at 60 °C for 20 min and then cooled in a cold-water bath for 5 min before adding 5 mL of glacial acetic acid. Finally, PNS concentration was measured at 545 nm using a spectrophotometer.

4.8. Characterization of complex hydrogels for ROS scavenging in vitro

A certain mass (1 g) dried sample was soaked in 1 mL PBS in a centrifuge tube and incubated in a water bath at 40 °C for 30 min. The mixture was then centrifuged at 6000 rpm for 10 min, and the supernatant was placed on ice for further testing. To the test tube, 50 μL of the supernatant and 950 μL of DPPH reagent were added. In the control tube, 50 μL of the supernatant and 950 μL of anhydrous ethanol were added, while the blank tube received 50 μL of PBS and 950 μL of DPPH reagent. Absorbance was measured using a UV spectrophotometer at a wavelength of 515 nm. The DPPH free radical scavenging rate was calculated using the following equation:

$$\text{DPPH Clear Rate} = \left(A_{blank} - A_{sample} + A_{control}\right) / A_{blank} * 100 \ \%$$

4.9. Evaluation of cytotoxicity and effect of hydrogels on cell behavior in vitro

HESCs and HUVEC were used to evaluate the cell cytotoxicity and cell proliferation. HESC was cultured at 37 °C in DMEM/F12 supplemented with 1 % P/S and 10 % FBS in a 5 % CO_2 atmosphere, and HUVEC was cultured at 37 °C in ECM supplemented with 1 % P/S, 1 % ECGS and 5 % FBS in a 5 % CO_2 atmosphere. RAW264.7 macrophage cells were used to evaluate the antioxidant efficiency of the hydrogels, and were cultured at 37 °C in DMEM supplemented with 1 % P/S and 10 % FBS in a 5 % CO_2 atmosphere. The hydrogel and the cell culture medium were co-cultured in the 37 °C constant temperature incubators at the ratio of 0.1 g/mL for 48h to obtain the hydrogels’ leach liquor.

Cell proliferation assay: HESCs and HUVEC were seeded into 96-well plates at a 1×10^3 cells/well density, and then different hydrogel extracts replace the normal cell culture medium. After being cultured for 1, 3, and 5 days, CCK-8 was added to each well and incubated for 2 h. Subsequently, the absorbance at a wavelength of 450 nm was measured using a microplate reader.

Cell cytotoxicity: HESCs was seeded into 6-well plates at a 1×10^5 cells/well density, and then different hydrogel extracts replace the normal cell culture medium. After being cultured for 1 and 3 days, Live/Dead staining was added to assess the cell cytotoxicity. Live cells were stained by Calcein-AM with green fluorescence, and the dead cells were stained by PI with red fluorescence.

Cell migration assay: HESCs were seeded into 6-well plates at a 3×10^5 cells/well density and cultured with the normal medium until reaching confluence. The 6-well plates were drawn with several parallel lines on the back in advance, and then the cells were scraped using the tip of a 200 μL micropipette perpendicular to the parallel line. After different time points co-cultured with the hydrogel extracts, images were captured again using the microscope. The cell migration rate was quantified by Image-J software, 5 random fields of view were selected within each group.

Tube formation Assays: The Matrigel was mixed with ECM medium at a 1:1 ratio and then 50 μL was added to each well of a 96-well plate and cultivated in a 37 °C cell incubator for 60 min. HUVEC that had been starved for 12 h was seeded into the 96-well plate on the surface on the Matrigel at a 4×10^4 cells/well density. After 4 h co-cultured with the different hydrogel extracts, images were captured using the microscope. The captured images were analyzed by ImageJ with the Angiogenesis Analyzer plugin.

Antioxidant efficiency: The experiment involved seeding RAW264.7 macrophage cells (1×10^5 cells in 1 mL of DMEM) into a 6-well plate. After 12 h of cell adherence, each group received a 6 h-exposure to different hydrogel extracts containing 100 μM H_2O_2. After rinsing three times with PBS, cells were treated with 10 μM 2′,7′-dichlorofluorescein diacetate (DCFH-DA) for 20 min. The H_2O_2 level of different incubation buffers was evaluated using a fluorescent microscope.

4.10. In vitro blood compatibility

A hemolysis activity assay was performed to evaluate the blood compatibility of the different hydrogels. In brief, whole blood was collected from healthy rats by sodium citrate collection tubes, then centrifuged at 4 °C, 3500 rpm for 5 min. The lower red blood cells were centrifuged another 3 times and re-suspended with 5 mL PBS. Then, 100 mg hydrogel samples were mixed with 1 mL erythrocytes in the tubes and placed in constant temperature and humidity incubator with 37 °C for 4 h. A negative control (PBS) and a positive control (Triton X-100) were also included in the experiment to calculate the degree of hemolysis. All of the samples were centrifuged at 3500 rpm for 5 min and the upper solution was taken to detect the absorbance at 545 nm by microplate reader. The hemolysis rate was calculated using the equation as follows:

$$\text{Hemolysis Rate }(\%) = \left(A_s - A_n / A_p - A_n\right) \times 100\%$$

Where A_p and A_n indicate the absorbance of the negative control and the positive control, respectively, As indicates the absorbance of the hydrogels samples.

4.11. In vitro antibacterial activity

Gram-positive bacteria (S. aureus) and Gram-negative bacteria (E. coli) were used as model bacteria to evaluate the *in vitro* antibacterial activity of the different hydrogels. Different hydrogels put in the 48-well plate and mixed with bacteria solution which concentration was 1×10^6 CFU/mL, the ratio was 0.1 g/mL. The orifice plates were placed in a constant temperature shaker and cultured at 37 °C、100 rmp for 6 h. At the end of the culture, the bacterial solution in each hole in the orifice plate was diluted 10,000 times. 100 μL of the diluted bacterial liquid was dropped on the solid medium and spread evenly. Put the culture in the incubator at 37 °C for 24 h. Finally, take photos of the solid medium, count the number of colonies on the medium, and calculate the survival rate. The experiment was repeated three times. The formula is as follows:

$$\text{Bacterial inhibition rate} = [1 - (N_s / N_c)] \times 100\%$$

In the formula, N_s was the number of colonies in the hydrogel sample group (CFU/mL), and N_c was the number of colonies in the control group (CFU/mL).

4.12. In vivo endometrial injury model construction and treatment

A rat model of endometrial injury was established by injecting 95 % ethanol into the uterus as described previously. In brief, pregnant horse serum was injected into the rats two days before the experiment to regulate the physiological cycle. After anesthetized with isoflurane, and the uterine horns were exposed via an abdominal incision. The sham-operated rats were injected in the uterine horns with 100 μL of saline. Rats in the control group and treatments group (CSMA, CSMA-RC, CSMA-RC-Zn-PNS) were injected in the uterine horns with 100 μL of 95 % ethanol, and distal portions of the uterus were clamped with vascular clamps to their full capacity and retained for 60 s to induce endometrial injury, and the uterine cavity was gently flushed with saline to remove residual ethanol. For the treatment's groups, 100 μL precursor hydrogel solutions were injected into the uterus, a US transducer was immersed into the solution, applying US for 60 s at 1 mm distance from the endometrial and 405 nm light irradiation was subsequently given. A US frequency of 25 kHz was used, and the hydrogels were administered as a single intraoperative injection, demonstrating *in vivo* adhesion and controlled degradation throughout the repair cycle.

Additionally, we conducted experiments involving US-only treatment and CSMA-RC-Zn-PNS monotherapy. Specifically, after establishing rat endometrial injury models, subjects received either US exposure (60 s) or CSMA-RC-Zn-PNS hydrogel injection alone, followed by surgical closure for postoperative recovery. Tissue samples were harvested at postoperative day 7 for endometrial repair assessment.

Finally, the muscle layer and skin were stitched using 5-0 unabsorbable sutures. Rats were euthanized at different time points after surgery, and the uterine tissues and blood were harvested for downstream analysis.

4.13. The effect of ultrasound on transdermal delivery efficiency in vivo

After the rat model of endometrial injury was established, the FITC-BSA labeled CSMA-RC-Zn-PNS precursor hydrogel solution was injected into the uterus, a US transducer was immersed into the solution, applying US for 60 s at 1 mm distance from the endometrial and 405 nm light irradiation was subsequently given. Another group prepared without US treatment were tested as the no-US control. Rats were euthanized immediately and 1 day after the surgery, the uterine tissues were collected for a frozen section and the nuclei were stained with DAPI. 1 mL of CSMA-RC-Zn-PNS hydrogel precursor solution was placed in a centrifuge tube. The US transducer was immersed in the solution for sonication, and a probe thermometer was inserted to record temperature changes.

4.14. Histologic and immunohistochemical analysis

The rat uterine were fixed in a 4 % paraformaldehyde solution for 72 h, after dehydration in graded concentration ethanol, then embedded in paraffin. Finally, tissue sections (5 μm) were mounted on slides for histological and immunohistochemical analysis.

The slices were baked at 65 °C for 1.5 h and then put in xylene for dewaxing and hydrated with graded concentration ethanol. Endometrial structure and thickness, number of glands were examined by H&E staining, and collagen deposition area was assessed by Masson staining.

For the immunohistochemical analysis, 1 × citrate buffer was prepared as the antigen repair solution, which was heated to >90 °C, and the tissue sections were placed in the citrate buffer for high-temperature repair for 20 min. After the repair, it was naturally cooled to room temperature. Sections were incubated for 16 h at 4 °C with different primary antibodies: Collagen I (1:200, ABclonal), α-SMA (1:200, ABcam), CK17 (1: 2000, CST), PCNA (1: 200, CST), CD31 (1:3000, ABcam), Vimentin (1:200, CST), ER (1: 200, ABcam) and PR (1: 200, ABcam). And then goat anti-rabbit serum was extracted from the rabbit two-step detection kit for incubation at 37 °C for 1 h, followed by DAB chromogenic reaction and hematoxylin staining. Image acquisition was performed under Panoramic Slide Scanners (3D HISTECH) and the percent positive rate were analyzed by ImageJ software.

4.15. Fertility and live birth assessment

After 5 weeks of the endometrial injury treatment surgery, the rats were anesthetized by isoflurane, the uterine horns were exposed via an abdominal incision and took photos to observe their status, and then sutured to continue feeding. One week later, SD male rats were paired 1:1 with the treatment female rats, and successful mating was confirmed by vaginal smear and the day was recorded as 0.5 days of gestation. Half rats were euthanized at the 21days of gestation, the number and rate of live births were observed, and the weight of the offspring was measured. Another half of the rats gave birth naturally and were continuously observed for subsequent growth of the fetal rats, and the maternal rats were executed three weeks later. Heart, liver, spleen, lung, kidney and blood were collected for downstream analysis.

4.16. Kidney, liver function and serum inflammatory factors assessment

Abdominal aortic blood was collected in tubes without anticoagulant in each group of rats. The serum was collected after centrifugation, then the serum concentrations of creatinine (CRE) and urea nitrogen (BUN) were measured to assess kidney function according to instructions of kidney function kits. Meanwhile, the serum concentrations of aspartate amino transferase (AST) and alanine amino transferase (ALT) were measured to assess the liver function according to instructions of liver function kits. The rat Elisa kit of IL-6, IL-1β, TNF-α were measured to assess the serum inflammatory factors change.

4.17. Statistical analysis

Statistical analysis was conducted using GraphPad Prism 9.0. Student's *t*-test was used to compare two groups, while one-way ANOVA followed by Bonferroni's tests was employed to compare three or more groups. $^{*}p < 0.05$, $^{**}p < 0.01$ and $^{***}p < 0.001$ were considered difference and significant difference, respectively, which was statistically significant, ns means no significance.

CRediT authorship contribution statement

Xin Zhang: Writing – original draft, Visualization, Resources, Methodology, Investigation, Formal analysis, Conceptualization. **Shufang Wang:** Writing – review & editing, Methodology, Investigation, Data curation. **Siyu Wang:** Software, Methodology, Formal analysis. **Zeyi Long:** Validation, Methodology, Data curation. **Cong Lu:** Resources, Formal analysis, Data curation. **Jianlin Wang:** Investigation, Formal analysis, Data curation. **Lijun Yang:** Methodology, Formal analysis, Data curation. **Cancan Yao:** Software, Formal analysis. **Bin He:** Supervision, Methodology, Conceptualization. **Xihua Chen:** Resources, Methodology, Investigation, Data curation. **Taifeng Zhuang:** Methodology, Funding acquisition, Formal analysis. **Xiangbo Xu:** Supervision, Project administration, Methodology, Funding acquisition, Formal analysis, Conceptualization. **Yufeng Zheng:** Writing – review & editing, Supervision, Project administration, Methodology, Investigation, Conceptualization.

Ethics approval and consent to participate

All protocols for animal care and treatment were approved by the Ethical Committee of National Research Institute for Family Planning (NRIFH 21-2308-3).

Declaration of competing interest

Yufeng Zheng is an editor-in-chief for Bioactive Materials and was not involved in the editorial review or the decision to publish this article. All authors declare that there are no competing interests.

Acknowledgements

Xin Zhang and Shufang Wang contributed equally to this work. This work was financially supported by the Non-profit Central Research Institute Fund of National Research Institute for Family Planning (2023GJZD01, 2023GJZ04), CAMS Innovation Fund for Medical (No. 2018-I2M-1–004).

Appendix A. Supplementary data

Supplementary data to this article can be found online at https://doi.org/10.1016/j.bioactmat.2025.04.007.

References

[1] S.A. Carson, A.N. Kallen, Diagnosis and management of infertility: a review, JAMA 326 (1) (2021) 65–76.

[2] J.L. Evers, Female subfertility, Lancet 360 (9327) (2002) 151–159.

[3] R.S. Magalhaes, J.K. Williams, K.W. Yoo, J.J. Yoo, A. Atala, A tissue-engineered uterus supports live births in rabbits, Nat. Biotechnol. 38 (11) (2020) 1280–1287.

[4] M. Carbonnel, P. Pirtea, D. de Ziegler, J.M. Ayoubi, Uterine factors in recurrent pregnancy losses, Fertil. Steril. 115 (3) (2021) 538–545.

[5] Y. Lin, S. Dong, W. Zhao, K.L. Hu, J. Liu, S. Wang, M. Tu, B. Du, D. Zhang, Application of hydrogel-based delivery system in endometrial repair, ACS Appl. Bio Mater. 3 (11) (2020) 7278–7290.

[6] C.J. Ang, T.D. Skokan, K.L. McKinley, Mechanisms of regeneration and fibrosis in the endometrium, Annu. Rev. Cell Dev. Biol. 39 (2023) 197–221.

[7] P. Rousselle, F. Braye, G. Dayan, Re-epithelialization of adult skin wounds: cellular mechanisms and therapeutic strategies, Adv. Drug Deliv. Rev. 146 (2019) 344–365.

[8] S. Capella-Allouc, F. Morsad, C. Rongières-Bertrand, S. Taylor, H. Fernandez, Hysteroscopic treatment of severe Asherman's syndrome and subsequent fertility, Hum. Reprod. 14 (5) (1999) 1230–1233.

[9] S. Guerriero, G. Condous, T. van den Bosch, L. Valentin, F.P. Leone, D. Van Schoubroeck, C. Exacoustos, A.J. Installé, W.P. Martins, M.S. Abrao, G. Hudelist, M. Bazot, J.L. Alcazar, M.O. Gonçalves, M.A. Pascual, S. Ajossa, L. Savelli, R. Dunham, S. Reid, U. Menakaya, T. Bourne, S. Ferrero, M. Leon, T. Bignardi, T. Holland, D. Jurkovic, B. Benacerraf, Y. Osuga, E. Somigliana, D. Timmerman, Systematic approach to sonographic evaluation of the pelvis in women with suspected endometriosis, including terms, definitions and measurements: a consensus opinion from the International Deep Endometriosis Analysis (IDEA) group, Ultrasound Obstet. Gynecol. 48 (3) (2016) 318–332.

[10] H. Ding, H. Zhang, R. Qiao, N. Sun, Y. Ji, W. Pang, W. Li, Q. Zhang, Comparing the efficacy and pregnancy outcome of intrauterine balloon and intrauterine contraceptive device in the prevention of adhesion reformation after hysteroscopic adhesiolysis in infertile women: a prospective, randomized, controlled trial study, Reprod. Biol. Endocrinol. 22 (1) (2024) 49.

[11] X.N. Lin, F. Zhou, M.L. Wei, Y. Yang, Y. Li, T.C. Li, S.Y. Zhang, Randomized, controlled trial comparing the efficacy of intrauterine balloon and intrauterine contraceptive device in the prevention of adhesion reformation after hysteroscopic adhesiolysis, Fertil. Steril. 104 (1) (2015) 235–240.

[12] L. Feng, Y. Sun, S. Zhang, Y. Qian, S. Fang, B. Yang, L. Xu, J. Li, Y. Niu, S. Zhang, L. Zhang, J. Chen, A novel intrauterine estrogen-releasing system for preventing the postoperative recurrence of intrauterine adhesion: a multicenter randomized controlled study, BMC Med. 22 (1) (2024) 395.

[13] D. Glujovsky, R. Pesce, C. Sueldo, A.M. Quinteiro Retamar, R.J. Hart, A. Ciapponi, Endometrial preparation for women undergoing embryo transfer with frozen embryos or embryos derived from donor oocytes, Cochrane Database Syst. Rev. 10 (10) (2020) Cd006359.

[14] Y.T. Song, P.C. Liu, J. Tan, C.Y. Zou, Q.J. Li, J. Li-Ling, H.Q. Xie, Stem cell-based therapy for ameliorating intrauterine adhesion and endometrium injury, Stem Cell Res. Ther. 12 (1) (2021) 556.

[15] Z. Yin, J. Wang, W. Cui, C. Tong, Advanced biomaterials for promoting endometrial regeneration, Adv. Healthcare Mater. 12 (16) (2023) e2202490.

[16] J. Cen, Y. Zhang, Y. Bai, S. Ma, C. Zhang, L. Jin, S. Duan, Y. Du, Y. Guo, Research progress of stem cell therapy for endometrial injury, Mater Today Bio 16 (2022) 100389.

[17] J. Fu, A. Warmflash, M.P. Lutolf, Stem-cell-based embryo models for fundamental research and translation, Nat. Mater. 20 (2) (2021) 132–144.

[18] E. Francés-Herrero, R. Lopez, M. Hellström, L. de Miguel-Gómez, S. Herraiz, M. Brännström, A. Pellicer, I. Cervelló, Bioengineering trends in female reproduction: a systematic review, Hum. Reprod. Update 28 (6) (2022) 798–837.

[19] J. Liao, X. Li, Y. Fan, Prevention strategies of postoperative adhesion in soft tissues by applying biomaterials: based on the mechanisms of occurrence and development of adhesions, Bioact. Mater. 26 (2023) 387–412.

[20] J. Ma, H. Zhan, W. Li, L. Zhang, F. Yun, R. Wu, J. Lin, Y. Li, Recent trends in therapeutic strategies for repairing endometrial tissue in intrauterine adhesion, Biomater. Res. 25 (1) (2021) 40.

[21] S.W. Choi, W. Guan, K. Chung, Basic principles of hydrogel-based tissue transformation technologies and their applications, Cell 184 (16) (2021) 4115–4136.

[22] H. Cao, L. Duan, Y. Zhang, J. Cao, K. Zhang, Current hydrogel advances in physicochemical and biological response-driven biomedical application diversity, Signal Transduct. Targeted Ther. 6 (1) (2021) 426.

[23] O. Chaudhuri, J. Cooper-White, P.A. Janmey, D.J. Mooney, V.B. Shenoy, Effects of extracellular matrix viscoelasticity on cellular behaviour, Nature 584 (7822) (2020) 535–546.

[24] T.E. Brown, K.S. Anseth, Spatiotemporal hydrogel biomaterials for regenerative medicine, Chem. Soc. Rev. 46 (21) (2017) 6532–6552.

[25] Y. Liang, J. He, B. Guo, Functional hydrogels as wound dressing to enhance wound healing, ACS Nano 15 (8) (2021) 12687–12722.

[26] R. Dimatteo, N.J. Darling, T. Segura, In situ forming injectable hydrogels for drug delivery and wound repair, Adv. Drug Deliv. Rev. 127 (2018) 167–184.

[27] T. Guan, J. Li, C. Chen, Y. Liu, Self-assembling peptide-based hydrogels for wound tissue repair, Adv. Sci. (Weinh.) 9 (10) (2022) e2104165.

[28] T. Vinikoor, G.K. Dzidotor, T.T. Le, Y. Liu, H.M. Kan, S. Barui, M.T. Chorsi, E. J. Curry, E. Reinhardt, H. Wang, P. Singh, M.A. Merriman, E. D'Orio, J. Park, S. Xiao, J.H. Chapman, F. Lin, C.S. Truong, S. Prasadh, L. Chuba, S. Killoh, S. W. Lee, Q. Wu, R.M. Chidambaram, K.W.H. Lo, C.T. Laurencin, T.D. Nguyen, Injectable and biodegradable piezoelectric hydrogel for osteoarthritis treatment, Nat. Commun. 14 (1) (2023) 6257.

[29] C. Yu, X. Ying, M.A. Shahbazi, L. Yang, Z. Ma, L. Ye, W. Yang, R. Sun, T. Gu, R. Tang, S. Fan, S. Yao, A nano-conductive osteogenic hydrogel to locally promote calcium influx for electro-inspired bone defect regeneration, Biomaterials 301 (2023) 122266.

[30] X. Jing, C. Xu, W. Su, Q. Ding, B. Ye, Y. Su, K. Yu, L. Zeng, X. Yang, Y. Qu, K. Chen, T. Sun, Z. Luo, X. Guo, Photosensitive and conductive hydrogel induced innerved bone regeneration for infected bone defect repair, Adv. Healthcare Mater. 12 (3) (2023) e2201349.

[31] F. Weinberger, I. Mannhardt, T. Eschenhagen, Engineering cardiac muscle tissue: a maturating field of research, Circ. Res. 120 (9) (2017) 1487–1500.

[32] D. Zhu, Z. Li, K. Huang, T.G. Caranasos, J.S. Rossi, K. Cheng, Minimally invasive delivery of therapeutic agents by hydrogel injection into the pericardial cavity for cardiac repair, Nat. Commun. 12 (1) (2021) 1412.

[33] L. Luo, Y. Li, Z. Bao, D. Zhu, G. Chen, W. Li, Y. Xiao, Z. Wang, Y. Zhang, H. Liu, Y. Chen, Y. Liao, K. Cheng, Z. Li, Pericardial delivery of SDF-1α puerarin hydrogel promotes heart repair and electrical coupling, Adv. Mater. 36 (1) (2024) e2302686.

[34] Y. He, Q. Li, P. Chen, Q. Duan, J. Zhan, X. Cai, L. Wang, H. Hou, X. Qiu, A smart adhesive Janus hydrogel for non-invasive cardiac repair and tissue adhesion prevention, Nat. Commun. 13 (1) (2022) 7666.

[35] M. Shahriari-Khalaji, M. Sattar, R. Cao, M. Zhu, Angiogenesis, hemocompatibility and bactericidal effect of bioactive natural polymer-based bilayer adhesive skin substitute for infected burned wound healing, Bioact. Mater. 29 (2023) 177–195.

[36] R. Fan, J. Zhao, L. Yi, J. Yuan, A. McCarthy, B. Li, G. Yang, J.V. John, W. Wan, Y. Zhang, S. Chen, Anti-inflammatory peptide-conjugated silk fibroin/cryogel hybrid dual fiber scaffold with hierarchical structure promotes healing of chronic wounds, Adv. Mater. 36 (16) (2024) e2307328.

[37] Z. Yang, R. Huang, B. Zheng, W. Guo, C. Li, W. He, Y. Wei, Y. Du, H. Wang, D. Wu, H. Wang, Highly stretchable, adhesive, biocompatible, and antibacterial hydrogel dressings for wound healing, Adv. Sci. (Weinh.) 8 (8) (2021) 2003627.

[38] M. Amiri, P. Khazaeli, A. Salehabadi, M. Salavati-Niasari, Hydrogel beads-based nanocomposites in novel drug delivery platforms: recent trends and developments, Adv. Colloid Interface Sci. 288 (2021) 102316.

[39] A.S. Mikhail, R. Morhard, M. Mauda-Havakuk, M. Kassin, A. Arrichiello, B. J. Wood, Hydrogel drug delivery systems for minimally invasive local immunotherapy of cancer, Adv. Drug Deliv. Rev. 202 (2023) 115083.

[40] J. Lin, Z. Wang, J. Huang, S. Tang, Q. Saiding, Q. Zhu, W. Cui, Microenvironment-protected exosome-hydrogel for facilitating endometrial regeneration, fertility restoration, and live birth of offspring, Small 17 (11) (2021) e2007235.

[41] X. Yi, F. Liu, K. Gao, F. Chen, Y. Wang, H. Li, X. Wang, Y. Huang, H. Fu, W. Zhou, J. B. Fan, S. Wang, Y. Gao, Reconstructable uterus-derived materials for uterus recovery toward efficient live births, Adv. Mater. 34 (8) (2022) e2106510.

[42] S. López-Martínez, A. Rodríguez-Eguren, L. de Miguel-Gómez, E. Francés-Herrero, A. Faus, A. Díaz, A. Pellicer, H. Ferrero, I. Cervelló, Bioengineered endometrial hydrogels with growth factors promote tissue regeneration and restore fertility in murine models, Acta Biomater. 135 (2021) 113–125.

[43] J. Qi, X. Li, Y. Cao, Y. Long, J. Lai, Y. Yao, Y. Meng, Y. Wang, X.D. Chen, H. Vankelecom, X. Bian, W. Cui, Y. Sun, Locationally activated PRP via an injectable dual-network hydrogel for endometrial regeneration, Biomaterials 309 (2024) 122615.

[44] H. Yang, G. Liu, C. Lu, Y. Zheng, X. Xu, J. Zhao, J. Li, Y. Xie, Z. Fang, Multifunctional group mediated double cross-linked polysaccharide complex hydrogel for microenvironmental regulation and repair of endometrial injury, Chem. Eng. J. 485 (2024) 149843.

[45] Q. Hu, N. Xie, K. Liao, J. Huang, Q. Yang, Y. Zhou, Y. Liu, K. Deng, An injectable thermosensitive Pluronic F127/hyaluronic acid hydrogel loaded with human umbilical cord mesenchymal stem cells and asiaticoside microspheres for uterine scar repair, Int. J. Biol. Macromol. 219 (2022) 96–108.

[46] Y. Zhu, S. Li, Y. Li, H. Tan, Y. Zhao, L. Sun, Antioxidant nanozyme microneedles with stem cell loading for in situ endometrial repair, Chem. Eng. J. 449 (2022) 137786.

[47] X. Zhang, G. Chen, Y. Wang, L. Fan, Y. Zhao, Arrowhead composite microneedle patches with anisotropic surface adhesion for preventing intrauterine adhesions, Adv. Sci. (Weinh.) 9 (12) (2022) e2104883.

[48] S. Li, Y. Li, F. Yu, N. Li, C. Liu, J. Mao, H. Sun, Y. Hu, Y. Zhu, M. Zhou, L. Ding, Human endometrium-derived adventitial cell spheroid-loaded antimicrobial microneedles for uterine regeneration, Small 18 (31) (2022) e2201225.

[49] Z. Ma, C. Bourquard, Q. Gao, S. Jiang, T. De Iure-Grimmel, R. Huo, X. Li, Z. He, Z. Yang, G. Yang, Y. Wang, E. Lam, Z.H. Gao, O. Supponen, J. Li, Controlled tough bioadhesion mediated by ultrasound, Science 377 (6607) (2022) 751–755.

[50] C.C. Yu, A. Shah, N. Amiri, C. Marcus, M.O.G. Nayeem, A.K. Bhayadia, A. Karami, C. Dagdeviren, A conformable ultrasound patch for cavitation-enhanced transdermal cosmeceutical delivery, Adv. Mater. 35 (23) (2023) e2300066.

[51] L. Xin, X. Lin, Y. Pan, X. Zheng, L. Shi, Y. Zhang, L. Ma, C. Gao, S. Zhang, A collagen scaffold loaded with human umbilical cord-derived mesenchymal stem cells facilitates endometrial regeneration and restores fertility, Acta Biomater. 92 (2019) 160–171.

[52] H. Lei, C. Zhu, D. Fan, Optimization of human-like collagen composite polysaccharide hydrogel dressing preparation using response surface for burn repair, Carbohydr. Polym. 239 (2020) 116249.

[53] L. Ding, G. Yan, B. Wang, L. Xu, Y. Gu, T. Ru, X. Cui, L. Lei, J. Liu, X. Sheng, B. Wang, C. Zhang, Y. Yang, R. Jiang, J. Zhou, N. Kong, F. Lu, H. Zhou, Y. Zhao, B. Chen, Y. Hu, J. Dai, H. Sun, Transplantation of UC-MSCs on collagen scaffold activates follicles in dormant ovaries of POF patients with long history of infertility, Sci. China Life Sci. 61 (12) (2018) 1554–1565.

[54] S. Shi, L. Wang, C. Song, L. Yao, J. Xiao, Recent progresses of collagen dressings for chronic skin wound healing, Collagen and Leather 5 (1) (2023) 31.

[55] D. Olsen, C. Yang, M. Bodo, R. Chang, S. Leigh, J. Baez, D. Carmichael, M. Perälä, E.R. Hämäläinen, M. Jarvinen, J. Polarek, Recombinant collagen and gelatin for drug delivery, Adv. Drug Deliv. Rev. 55 (12) (2003) 1547–1567.

[56] W. Liu, H. Lin, P. Zhao, L. Xing, J. Li, Z. Wang, S. Ju, X. Shi, Y. Liu, G. Deng, G. Gao, L. Sun, X. Zhang, A regulatory perspective on recombinant collagen-based medical devices, Bioact. Mater. 12 (2022) 198–202.

[57] M. Godoy-Gallardo, U. Eckhard, L.M. Delgado, Y.J.D. de Roo Puente, M. Hoyos-Nogués, F.J. Gil, R.A. Perez, Antibacterial approaches in tissue engineering using metal ions and nanoparticles: from mechanisms to applications, Bioact. Mater. 6 (12) (2021) 4470–4490.

[58] W. Wang, K.W.K. Yeung, Bone grafts and biomaterials substitutes for bone defect repair: a review, Bioact. Mater. 2 (4) (2017) 224–247.

[59] A. Sirelkhatim, S. Mahmud, A. Seeni, N.H.M. Kaus, L.C. Ann, S.K.M. Bakhori, H. Hasan, D. Mohamad, Review on zinc oxide nanoparticles: antibacterial activity and toxicity mechanism, Nano-Micro Lett. 7 (3) (2015) 219–242.

[60] Y.Y. Yu, D.D. Fan, Coordination study of recombinant human-like collagen and zinc (II), Spectrochim. Acta Mol. Biomol. Spectrosc. 81 (1) (2011) 412–416.

[61] S. Jia, J. Wang, S. Li, X. Wang, Q. Liu, Y. Li, M. Shad, B. Ma, L. Wang, C. Li, X. Li, Genetically encoded zinc-binding collagen-like protein hybrid hydrogels for wound repair, Int. J. Biol. Macromol. 254 (Pt 1) (2024) 127592.

[62] A.D. Gholap, S. Rojekar, H.S. Kapare, N. Vishwakarma, S. Raikwar, A. Garkal, T. A. Mehta, H. Jadhav, M.K. Prajapati, U. Annapure, Chitosan scaffolds: expanding horizons in biomedical applications, Carbohydr. Polym. 323 (2024) 121394.

[63] Z. Shariatinia, Pharmaceutical applications of chitosan, Adv. Colloid Interface Sci. 263 (2019) 131–194.

[64] J. Yao, Y. Chen, X. Zhang, J. Chen, C. Zhou, J. Jiang, H. Zhang, K. Wu, Slightly photo-crosslinked chitosan/silk fibroin hydrogel adhesives with hemostasis and anti-inflammation for pro-healing cyclophosphamide-induced hemorrhagic cystitis, Mater Today Bio 25 (2024) 100947.

[65] H. Zhang, Y. Cong, A.R. Osi, Y. Zhou, F. Huang, R.P. Zaccaria, J. Chen, R. Wang, J. Fu, Direct 3D printed biomimetic scaffolds based on hydrogel microparticles for cell spheroid growth, Adv. Funct. Mater. 30 (13) (2020) 1910573.

[66] C. Yang, L. Qu, R. Wang, F. Wang, Z. Yang, F. Xiao, Multi-layered effects of Panax notoginseng on immune system, Pharmacol. Res. 204 (2024) 107203.

[67] H. Zhong, H. Wu, H. Bai, M. Wang, J. Wen, J. Gong, M. Miao, F. Yuan, Panax notoginseng saponins promote liver regeneration through activation of the PI3K/AKT/mTOR cell proliferation pathway and upregulation of the AKT/Bad cell survival pathway in mice, BMC Compl. Alternative Med. 19 (1) (2019) 122.

[68] G. Bao, Q. Fan, D. Ge, M. Sun, H. Guo, D. Xia, Y. Liu, J. Liu, S. Wu, B. He, Y. Zheng, In vitro and in vivo studies on magnesium alloys to evaluate the feasibility of their use in obstetrics and gynecology, Acta Biomater. 97 (2019) 623–636.